IEEE Robotics and Automation Letters (RA-L) paper, presented at ICRA 2023, London, UK. Cite as RA-L paper.

Velocity following control of a pseudo-driven wheel for reducing internal forces between wheels

Huanan Qi[1], Liang Ding[1], Bo You[2], Lan Huang[1], Xin An[1], Shu Li[1], and Guangjun Liu[3]

***Abstract*—The coordination of multiple driving wheels is an important issue in wheeled mobile robot design, for both maximizing tractive capability and optimizing energy consumption. This study converts a driving wheel into a pseudo-driven wheel (PDW), which is controlled to follow the motion of the robot body, in accordance with the kinematic constraints. To eliminate the internal force conflicts between wheels, a velocity following control (VFC) method is proposed to control the PDW in the presence of force disturbance caused by soil distortion during wheel-terrain interaction. The feasibility of the PDW conversion and the proposed control method are experimentally demonstrated. Compared with the inverse kinematics control (IKC) method, the rover using PDW with VFC is shown to be capable of more accurate straight and steering path following on soft terrain, reducing internal forces between wheels by more than 70% in the experiments.**

***Index Terms*—Wheeled mobile robot, pseudo-driven wheel, velocity following control, kinematic constraint.**

I. Introduction

WHEELED mobile robots (WMRs) have been—or are planned to be—used for exploring planets and other astronomical bodies such as Mars and the Moon, and their deformable terrains pose difficult challenges [1], [2]. Increasing the number of driving wheels can reduce the load on each wheel, which in turn helps decrease wheel sinkage and slip, thus improving the WMR tractive capability [3]. However, this creates a redundant driving system [4] in which the coordination between driving wheels becomes an important issue, both in fully exerting the tractive capability and in optimizing energy consumption.

A substantial amount of work on improving the coordination between wheels has been presented, focusing on the optimization of the wheels' slip ratios and driving torque. Yoshida and Hamano [5] have demonstrated that each individual wheel can reach its maximum driving efficiency when the slip ratios of all the driving wheels are reduced by decreasing the excess force on the tires. A fuzzy proximity control method to achieve wheel coordination control has been reported, which considers the hook traction and resistance torque factors [6], [7], but requires accurate dynamic models. In [8], the wheel torque was distributed to optimize energy consumption and maximize traction. However, the wheel-terrain contact angles of all wheels must be known. Additionally, a wheel-torque control approach was analyzed in [9], which aims to optimize the distribution of the wheel driving torque by solving a set of constrained optimization problems. However, the authors did not consider the interaction between the various body parts. Considering the parasitic power losses in mobile robots, people defined the instantaneous power as the optimization target [10] and presented equal-slip-rate control as a feasible suboptimal solution. The functional relationship between the resistance torque coefficient and slip ratio was analyzed in [11].

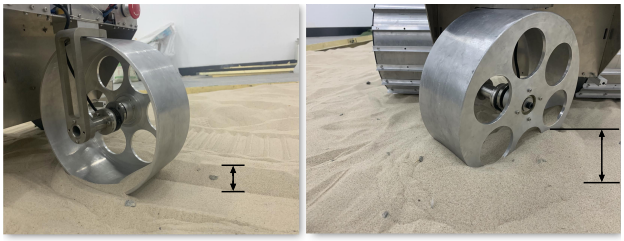

(a) The driven wheel moves forward (b) The driven wheel moves backward

Fig. 1: Bulldozing state of a driven wheel on soft terrain.

The above-mentioned methods require solving complex terramechanics equations with highly coupled integral terms. The accuracy of these models rely on the existence of accurate parameters of the terrain and wheels, which are difficult to determine when the WMR is deployed to—or enters—new, unknown environments. In fact, the effects of terrain deformation in the WMR's dynamics could be regarded as unknown force disturbances, and compensated by active disturbance rejection controllers (ADRCs). Separability principles of ADRC and independent model characteristics have been proved in [12]–[14]. Furthermore, successful experience on the ADRC used in a path following has been reported in [15].

In addition, designers and researchers tend to replace one or more driving wheels with driven wheels which have no driving mechanism, to achieve the coordinate motion of wheels [16]. However, this replacement leads to larger tracking resistance for the rover in deformable terrains. The effect of the rear

Manuscript received: August, 01, 2021; Revised November, 28, 2021; Accepted January, 24, 2022.

This paper was recommended for publication by Editor Pauline Pounds uponevaluation of the Associate Editor and Reviewers' comments. This work was supported by the National Natural Science Foundation of China (Grants No. 91948202, 52005122, 51822502, and 431020301), National Key Research and Development Program of China (Grant No. SQ2019YFB130016), Fundamental Research Funds for the Central Universities (Grant No. FRFCU9803500621) and the '111' Project (Grant No. B07018). (*Corresponding author:* Liang Ding, Bo You.)

[1]Huanan Qi, Liang Ding, Lan Huang, Xin An, and Shu Li are with the Harbin Institute of Technology, Heilongjiang, 150001, China huananqi@outlook.com; liangding@hit.edu.cn; huanglanxyz@163.com; andyan98@163.com; li_shu43@hotmail.com.

[2]Bo You is with school of Automation, Harbin University of Science and Technology, Heilongjiang, 150080, China youbo@hrbust.edu.cn.

[3]Guangjun Liu is with the Department of Aerospace Engineering, Ryerson University, Toronto, ON M5B 2K3, Canada gjliu@ryerson.ca.

Digital Object Identifier (DOI): 10.1109/LRA.2022.3150018

driven wheel of a three-wheeled mobile robot moving on soft terrain is shown in Fig. 1, in which arrow lines in the figure show the amplitude of the wheel bulldozing effect. In such conditions, internal forces between wheels will be generated. The concept of a pseudo-driven wheel (PDW) was presented and its control strategy on adjusting the number of degrees of freedom was studied in the previous work [17]. The present study focuses on reducing the magnitude of internal conflicting forces between the wheels. A fast neural network control was proposed to improve the disturbance compensation of a PDW in different terrain [18], but the advantage of the velocity closed loop by the force was not analyzed independently.

This paper proposes an effective method to improve the coordinated control of WMR motion by eliminating the internal force conflicts between wheels. The performance of a PDW applied to WMRs in reducing internal forces between wheels was investigated. Kinematic constraints of a PDW are combined with the simplified model of WMRs for the inverse kinematics control (IKC). Moreover, the force disturbances resulting from terrain deformation during the wheel-terrain interaction are compensated using a velocity following control (VFC) with ADRCs, which is used for converting a normal driving wheel into PDW, without using dynamic models. The proposed control methods are experimentally validated, and the experimental results show that the VFC method reduces the internal forces between wheels more effectively than the IKC when the WMR followed the same path but could be different velocities.

The main contributions of this work are summarized below.

1) Internal force between wheels is substantially reduced based on the concept of PDW. A VFC method is developed to implement passive control of the driving wheels, taking into account the wheel-terrain interaction.
2) Inverse kinematic control of the robot is implemented by the given PDW kinematics constraints as a comparison. It has been demonstrated that the VFC can effectively relax the internal conflicting force between wheels, and it can also reduce the energy consumption of the robot.

The rest of this paper is organized as follows. Modeling of the PDW is presented in Section II, and Section III discusses the design of the velocity following control system. Experimental results are presented in Section IV to validate the proposed controllers. Section V concludes the paper.

II. Modeling of a Pseudo-Driven Wheel

The instantaneous planar motion of an arbitrary multi-wheeled mobile robot on flat terrain can be made equivalent to that of a two-wheeled one. A three-wheeled mobile robot, which is the simplest multi-wheel drive system, is used here as an example to perform the PDW application. In Fig. 2, r and d_1 are the radius and distance between the geometric center and wheel center, respectively; ω_b and v_b are the body's angular and linear velocities, respectively; ω_i and v_i, $i = 1, 2, 3$, are the angular velocity of wheel i and the velocity generation at the ith wheel center, respectively; ϕ and φ are the steering angles of the body and rear wheel, respectively; R_1 and R_2 are the circular motion radii of the left and rear wheels, respectively; finally, L is the wheel base length.

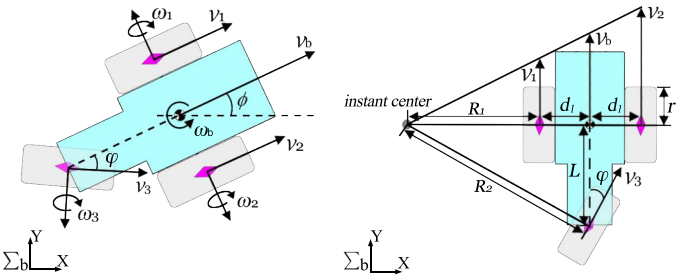

(a) Body's motion analysis model (b) Body's geometric analysis model

Fig. 2: Body's kinematic state analysis model.

Given that all the wheels of the WMR are rigidly connected, their linear velocities satisfy the motion constraint:

$$\frac{v_1}{R_1} = \frac{v_2}{R_1 + 2d_1} = \frac{v_3}{R_2}. \tag{1}$$

Under this kinematic relationship, the WMR's velocity can be calculated by the rotation velocity of any arbitrary two wheels. Here, we choose a pair of symmetrically distributed wheels: the left and right wheels of the WMR. The simplified inverse kinematics can then be written as follows [19]:

$$\begin{bmatrix} \dot{x} \\ \dot{y} \\ \dot{\phi} \end{bmatrix} = \begin{bmatrix} \frac{r\cos\phi}{2} & \frac{r\cos\phi}{2} \\ \frac{r\sin\phi}{2} & \frac{r\sin\phi}{2} \\ \frac{r}{2d_1} & \frac{r}{2d_1} \end{bmatrix} \begin{bmatrix} \omega_1(1-s_1) \\ \omega_2(1-s_2) \end{bmatrix}, \tag{2}$$

where s_1 and s_2 are the slip ratios of the left and right wheels, respectively.

The third driving wheel is converted to a driven wheel that actively follows the motion of the WMR. Under ideal conditions, this wheel does not slide, and its steering angle φ satisfies the following kinematic constraint:

$$\varphi = \arctan \frac{L(\omega_2 - \omega_1)}{d_1(\omega_2 + \omega_1)}. \tag{3}$$

The two driving wheels are symmetrically located on the two sides of the WMR, and can be regarded as the dominant driving wheels that determines the WMR motion, with the remaining wheels actively following the body motion [using the IKC (1) and (3)] without generating any resistance, sliding forces, or unrequited drawbar pull, thus avoiding kinematic incoordination and internal forces.

Remark 1: A pseudo-driven wheel is a driving wheel that actively follows the body movement without generating any forces to it in the motion plane, while supporting the body of the robot like a driven wheel.

The use of PDWs can reduce the modeling dimensions of WMR models, and decrease the internal force conflicts between wheels, thus reducing energy consumption. Note that a PDW should comply with the rules of two-degrees-of-freedom motion, in order to encompass more general situations, including applications in full-fledged planetary exploration rovers. For example, when the WMR is steering, the PDW needs to also adjust its steering angle accordingly. This can be done using either an actuator or a passive steering mechanism.

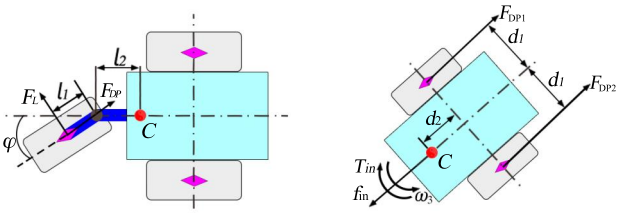

(a) Forces on the pseudo-driven wheel collected by the force sensors

(b) Internal force and torque between the pseudo-driven wheel and the body

Fig. 3: Forces on the PDW and between the PDW and body.

What's more, to provide better support and tracking of the body movements, the PDW could have more degrees of freedom (e.g., vertical movement).

III. Velocity following control of a PDW

This section considers more wheel-terrain interaction for designing an adaptive control scheme than the IKC method. The proposed VFC method and its design are presented.

A. Internal Forces Between the PDW and the Robot Body

The force on the PDW and the internal forces between the wheel and the body in a three-wheeled mobile robot are shown in Fig. 3, where C is the center of mass, F_{DP} and F_L are the drawbar pull and lateral force on the wheel, respectively, φ is the wheel steering angle, l_1 and l_2 are the distances between the wheel center and steer axis and that between the steer axis and centroid, respectively, and f_{in}, T_{in} are the internal force and torque between the PDW and body, respectively.

The internal force, and torque around the vertical, between the PDW and body are given by (4) below:

$$\begin{cases} f_{in} = -F_{DP}\cos\varphi + F_L\sin\varphi \\ T_{in} = (F_{DP}\sin\varphi + F_L\cos\varphi)(l_1\cos\varphi + l_2) \end{cases}. \quad (4)$$

From (4), the control objective of reducing the internal forces can be achieved by eliminating the F_{DP} and F_L.

Remark 2: Given the symmetrical structure of the three-wheeled mobile robot, the internal forces f_{in}, T_{in} are equivalent to the composition of internal forces between the wheels.

B. Velocity Following Force Approach

The velocity following force approach is based on reducing the internal forces (f_{in}, T_{in}) between the PDW and the robot body, thus effectively performing passive following control. Any path can be considered as a combination of straight and steering sub-paths. The movements of the PDW using the VTF is shown in Fig. 4. A coordinate system is established, with the PDW advancing direction as the x-axis, using a clockwise rule in the horizontal plane. The relationships between the velocity generation v of the wheel, steering angle φ, and forces F_{DP}, F_L are discussed below.

1) PDW in straight-path motions: The force sensor at the wheel's axle measures negative values along the x-axis, indicating that the wheel is subjected to resistance. The velocity generation at the wheel should therefore be increased. The slip-rate of the wheel is also increased, because the body velocity does not change. According to the Janosi model, the

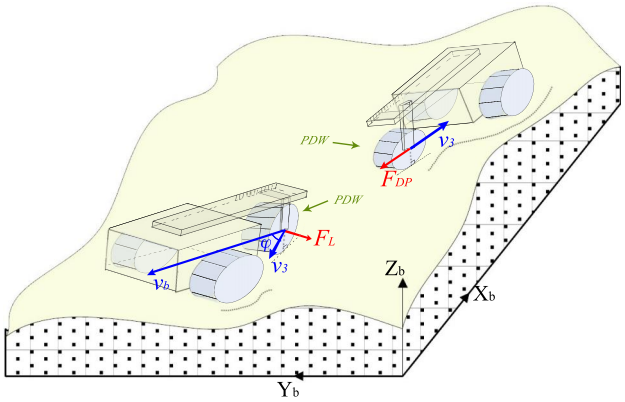

Fig. 4: Motions of the PDW using velocity following control.

relationship between the soil shear stress τ and slip ratios s is given by [20],

$$\tau(\theta) = [c + \sigma(\theta)\tan\Phi][1 - e^{-r[(\theta_1'-\theta)-(1-s)(sin\theta_1'-sin\theta)]/K}], \quad (5)$$

where c is the soil cohesion, Φ is the internal friction angle, K is the shearing deformation modulus, and σ is normal stress determined by the approach angle θ_1.

Based on Eq.(5) and experimental results of [20], the increased slip-rate of the wheel causes an increase in the soil shear stress τ, within a certain range. The drawbar pull F_{DP} is therefore increased, which decreases the resistance on the wheel according to the wheel-terrain interaction force (6).

$$F_{DP} = -rb\int_{\theta_2}^{\theta_1}\sigma(\theta)\sin\theta d\theta + rb\int_{\theta_2}^{\theta_1}\tau(\theta)\cos\theta d\theta. \quad (6)$$

where θ_1 is the approach angle, θ_2 is the departure angle, r is the wheel radius, and b is the wheel width.

The same mechanism applies to the case of the force sensor returning a positive value.

2) PDW in steering-path motions: When the steering angle φ of the wheel is the inappropriate position, such as when the body turns or slips sideways, there will be an angle between the body's traveling velocity vector and wheel's velocity vector, which causes the PDW to slip. In this instance, the force sensor measurement along the y-axis will not be zero. Therefore, the steering angle of the PDW will be adjusted to make the lateral force F_L zero, which brings the PDW to the correct alignment.

We can therefore conclude that the intended velocity tracking can be achieved by enforcing $F_{DP} = 0$ and $F_L = 0$.

C. Compensating for the Resistance Resulting From Terrain Deformation

ADRCs are used to compensate for the total disturbances, which requires knowledge of the order of the system.

1) Derivation of the system state equation: The wheel-soil interaction of a planetary rover is shown in Fig. 5, where W is the equivalent vertical load on the wheel, F_N is the normal force, T is the driving torque, ω_w, v_w are the wheel angular and linear velocities, respectively, and θ_m, z, and l are wheel-terrain interaction model parameters [21].

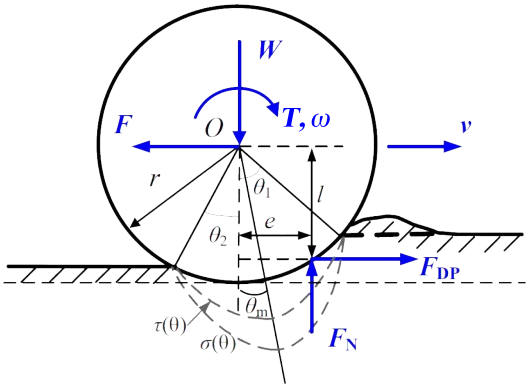

Fig. 5: Forces on the wheel-soil interaction of a rover.

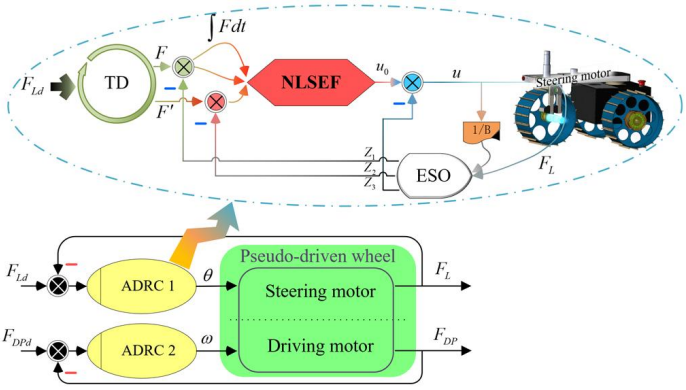

Fig. 6: Decoupling of the ADRC control system.

The torque on a wheel can be written as [16]:

$$T = F_{DP}r + F_N rRC, \tag{7}$$

where RC is the resistance torque coefficient.

The wheel rotational dynamics can be written as

$$I\dot{\omega} = T - T_R, \tag{8}$$

where I is the rotational inertia, and T_R the resistance torque.

As determined by Gao *et al.* [11], the value of the resistance torque can be obtained by fitting the experimental results with an exponential function of the form,

$$T_R = a_R^{s^{b_R}} F_N r + c_R F_N r, \tag{9}$$

where T_R is the resistance torque, and a_R, b_R, and c_R are wheel parameters.

Considering (7), (8), and (9), a dynamic equation containing the mechanics of the wheel-soil interaction can be obtained:

$$I\dot{\omega} = F_{DP}r + F_N r(RC - a_R^{s^{b_R}} - c_R), \tag{10}$$

where ω is the control input, and the optimized force F_{DP} is the system output, which is tracked with an improved ADRC. Then, a simplified dynamic model can also be obtained:

$$F_{DP} = \frac{I}{r}\ddot{\omega} + f(F_N, s), \tag{11}$$

which can be rewritten as

$$\ddot{q} = f(F_N, s, \delta) + B\dot{u}, \tag{12}$$

where q is the angular displacement, B is an input constant, u is the force measured by a force sensor, $f(F_N, s, \delta)$ is an additional state variable, and δ is the uncertainty in the model. As seen in (12), this is a second-order system.

2) Design of the Model-Free ADRCs: The system based on the presented internal force calculation (4) can be decoupled into two second-order subsystems, as shown in Fig. 6: the first one to control the lateral force F_L, and the other to control the drawbar pull F_{DP}. The set of parameters for each of the particular subsystems requires only small adjustments when applied to the other, because of the structure similarity between them. Therefore, the design procedure for the force F_L of the PDW is described next, as an example, with the structure of its controller being shown in Fig. 6.

The overall control scheme consists of three parts: tracking differentiator, extended state observer, and nonlinear state error feedback law. The details are as follows:

a) Tracking differentiator: The input signal mutation can be smoothened by tracking differentiator (TD), alleviating the conflict between rapidity and overshooting. Both the desired input and its approximate differential signal can be tracked by

$$\begin{cases} fh = fhan(x_1 - x_d, x_2, r_0, h_0), \\ x_1(k+1) = x_1(k) + hx_2(k), \\ x_2(k+1) = x_2(k) + hfh, \end{cases} \tag{13}$$

where x_d is the first-order system state to be approximated, x_1 and x_2 are the desired input and its differential signal, respectively, and $fhan\ (x_1, x_2, r_0, h_0)$ is the time-optimal control comprehensive function defined by Han [22] as

$$\begin{cases} d = r_0 h_0^2,\ a_0 = h_0^2 x_2,\ y = x_1 + a_0 \\ a_1 = \sqrt{d(d + 8|y|)}, \\ a_2 = a_0 + sign(y)(a_1 - d)/2, \\ fsg(x, d) = (sign(x + d) - sign(x - d))/2, \\ a = (a_0 + y)fsg(y, d) + a_2(1 - fsg(y, d)), \\ fhan = -r_0(\dfrac{a}{d})fsg(a, d) + r_0 sign(a)(1 - fsg(a, d)), \end{cases} \tag{14}$$

where r_0 and h_0 are controller parameters, and h denotes the sampling period.

b) Extended state observer: The core functions of the ADRC are the estimation and compensation of the total disturbance, which consists of unknown parts in the system model. Treating $f(\cdot)$ as an additional state variable, $x_3 = f(\cdot)$, the original plant (12) can be described as

$$\begin{cases} x_1 = q,\ x_2 = Bu,\ x_3 = f(\cdot), \\ \dot{x}_1 = x_3 + \dot{x}_2, \\ y = x_1. \end{cases} \tag{15}$$

A state observer in discrete form for second-order systems, denoted as the nonlinear extended state observer (ESO), was proposed by Gao [23] as

$$\begin{cases} e(k) = z_1(k) - y(k), \\ z_1(k+1) = z_1(k) + h(z_2(k) - \beta_1 e(k)), \\ z_2(k+1) = z_2(k) + h(z_3(k) - \beta_2 fal(e, 0.5, h)), \\ z_3(k+1) = z_3(k) + h(-\beta_3 fal(e, 0.25, h)), \end{cases} \tag{16}$$

where $z_1 \to x_1$, $z_2 \to x_2$, and $z_3 \to x_3$ denote the observed values, and β_1, β_2, and β_3 are tuning parameters.

The objective of the ESO is the estimation of z_3, which can then be used to compensate the input u, and calculate the input errors of the nonlinear state error feedback law. The expansible state z_3 is mainly the force disturbance caused by soil distortion during wheel-terrain interaction, and a part of the uncertainty of the approximation model.

c) Nonlinear state error feedback law: While the tracking error can be made to converge to zero by using a linear feedback combination PID controller, the speed of convergence may not be satisfactory without resorting to high gains. In contrast, according to a study by Han [22], significant performance and efficacy can be achieved in the controller by using nonlinear feedback. Therefore, a nonlinear state error feedback (NLSEF) was used, to provide better results, based on the following function presented in [24]:

$$fal(e,\alpha,\varepsilon) = \begin{cases} \frac{e}{\delta^{1-\alpha}}, & |x| < \varepsilon \\ |e|^{\alpha} sign(e), & |x| \geq \varepsilon, \end{cases} \tag{17}$$

where e denotes the error, and α and δ are parameters.

Considering the nonlinear feedback, the inputs can be written as in (18):

$$\begin{aligned} u_0(k+1) = u_0(k) + k_p fal(e_1,\alpha_1,\varepsilon_1) + k_I \textstyle\sum_{i=1}^{n} fal(e_1,\alpha_1,\varepsilon_1) \\ + k_D fal(e_2,\alpha_2,\varepsilon_2), \end{aligned} \tag{18}$$

where k_p, k_I, and k_D denote the proportional, integral, and derivative gains of the controller, respectively.

The overall control law is obtained by combining the above three parts [Eqs. (13), (16), (18)]. However, setting its parameter values is a hard problem, which generally needs to be solved through practice. Han [22] presented a relationship between the ESO parameters and a Fibonacci sequence, and Gao [23] proposed a method for setting the parameters according to the system bandwidth. In particular, the high-gain parameters show a special advantage in our designing. The parameter set related to Han's approach is given in $r_0 = 50$, $h_0 = h$ $\beta_1 = 1/h$, $\beta_2 = 1/3h^2$, $\beta_3 = 1/32h^3$, $\alpha_1 = 0.75$, $\alpha_2 = 0.67$, $\varepsilon_1 = \varepsilon_2 = 2h$, $k_{P1} = 0.17$, $k_{I1} = 0.67$, $k_{D1} = 0.20$, $k_{P2} = 0.30$, $k_{I2} = 0.70$, $k_{D2} = 0.40$.

The overall control system uses two ADRC subsystems to eliminate the drawbar pull F_{DP} of the PDW and the lateral force F_L, respectively.

IV. Experimental Validation

This section experimentally validates the application of a PDW on a WMR, and evaluates the performance of the VFC and IKC by analysing twelve trail results of three tasks.

A. Experimental Setup

The experimental setup was designed to physically validate the defined PDW concept, and its control method on a velocity-controlled three-wheeled mobile robot with four brush DC motors (FAULHABER 3257G024CR) and three six-axis force sensors (SRI 3705C) depicted in Fig. 7. One motor and one sensor were mounted on each front wheel, and two motors

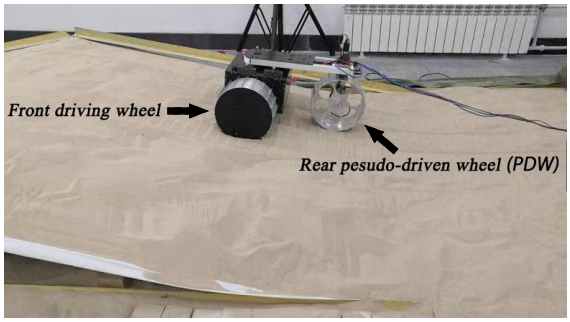

Fig. 7: Experimental three-wheeled rover on soft terrain.

and one sensor in the PDW. Each motor had an absolute encoder (HEDM 5540). The chassis and PDW were linked by a bracing frame, and the PDW had a single support arm on the right side. One of the motors on the PDW was working on velocity control mode and the other worked in position control mode, to provide drive and steering power, respectively. The front motors worked in velocity control mode.

The sampling period of the ADRC was chosen as $h = 0.01$, and the other parameters were set as subsection III-C. The parameters for the kinematic constraint equations [see (2), (3)] were chosen as $r = 140$ mm, $d = 250$ mm, $l = 446$ mm, $s_1 = 0$ and $s_2 = 0$. The parameters for the calculated internal forces [see (4)] were $l_1 = 31.16$ mm and $l_2 = 364.61$ mm.

B. Experimental Results

Three different robotic tasks were tested: straight motion on flat (Task 1) and sloping (Task 2) soft sandy terrain, and steering motion (Task 3) on flat soft sandy terrain. A 10 degrees inclination was used in Task 2. In Task 1 and Task 2, the body traveling velocity was set to the same value used for the Jade Rabbit lunar rover: $v_b = 55$ mm/s [25]; in Task 3, the desired body angular velocity was set to $\omega_d = 0.2$ rad/s. Eight trials were carried out for each task, and all collected data of trails were shown in below figures. Then the average calculation is used to fit each four trails' data into one curve.

1) Sensor data: When driving wheels have no velocity compensation control, the WMR slip phenomenon [described by (19)] is serious on soft terrain, causing the real velocity v_r lower than the older v_d. Holding the slip is being judged important for studying the wheel-terrain interaction by scholars. At this point, a PDW is equipped in the rover to supporting the body without generating velocity and force effect almost to front wheels, which will be more conducive to study the interaction than single wheel experiments [20].

$$s = \frac{v_d - v_r}{v_d}. \tag{19}$$

In terms of velocity, as seen in Figs. 8(a), (e), and (i), the resulting VFC values are always lower than the command. Because the PDW using the VFC adaptively follows the body movement based on a force sensor. This means that no additional velocity was provided to the body. However, IKC needs to use external sensors to achieve the same effect. The real velocity of the rover is measured by a driving ruler and a program timer, $v_{rVFC} = 49.51$, 11.28 mm/s of the Task 1

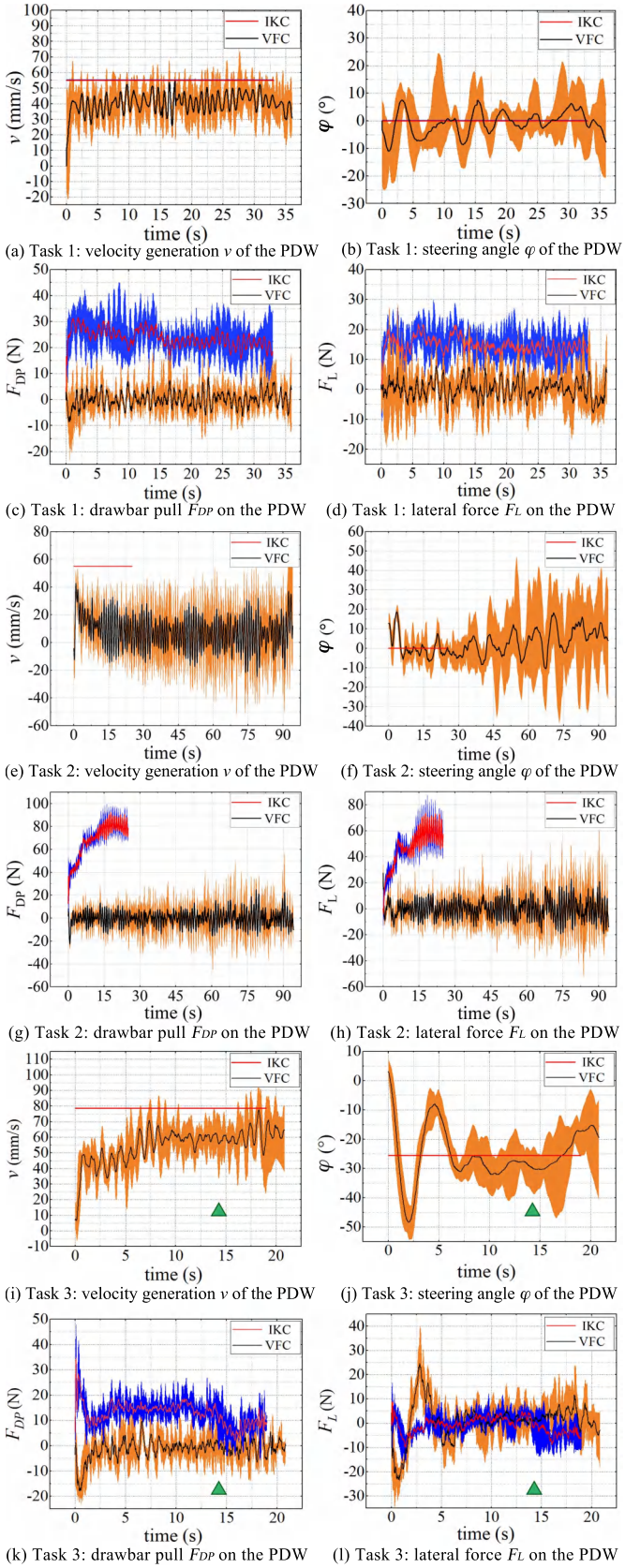

(a) Task 1: velocity generation v of the PDW (b) Task 1: steering angle φ of the PDW
(c) Task 1: drawbar pull F_{DP} on the PDW (d) Task 1: lateral force F_L on the PDW
(e) Task 2: velocity generation v of the PDW (f) Task 2: steering angle φ of the PDW
(g) Task 2: drawbar pull F_{DP} on the PDW (h) Task 2: lateral force F_L on the PDW
(i) Task 3: velocity generation v of the PDW (j) Task 3: steering angle φ of the PDW
(k) Task 3: drawbar pull F_{DP} on the PDW (l) Task 3: lateral force F_L on the PDW

Fig. 8: Velocity, angle, and forces on the PDW in the tasks.

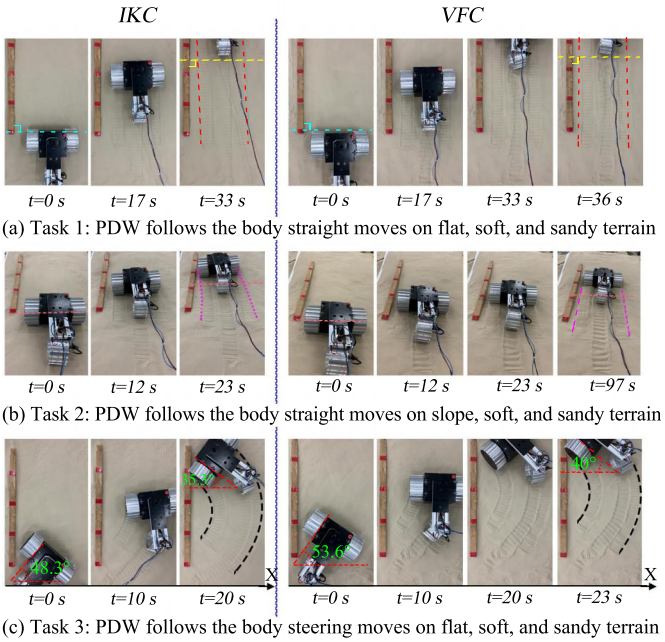

(a) Task 1: PDW follows the body straight moves on flat, soft, and sandy terrain
(b) Task 2: PDW follows the body straight moves on slope, soft, and sandy terrain
(c) Task 3: PDW follows the body steering moves on flat, soft, and sandy terrain

Fig. 9: PDW following the body motion during the three tasks. The outer diameter between the front and rear wheels is 700 mm. The distance between every two red marks on the board is 400 mm.

and 2, and $v_{rIKC} = 54.62$, 47.13 mm/s, respectively. These are further calculated by (19), $s_{VFC} = 0.1$ and $s_{IKC} = 0.01$ in Task 1, and $s_{VFC} = 0.79$ and $s_{IKC} = 0.14$ in Task 2. Based on experimental experiences that the normal slip is about s>0.6 in such sloping motion [21], these results indicate that the PDW using the VFC has less influence on the front wheel movement. In addition, in terms of force, as shown in Figs. 8(c), (g), (k), these two approaches produce very different forces on the PDW. The drawbar pull F_{DP} of the VFC, in the range $F_{DP} = -22.6$ to 24.8 N in Task 2, is much smaller than that of the IKC, which is the range $F_{DP} = 12.8$ to 99.0 N, especially. In fact, it shows that the PDW using the IKC is pushing the front wheels. It is undesired in the design, while the wheel with IKC can increase the traction of the WMR, because of the large internal force between the wheels.

On soft sandy terrain, the different slip ratios of the front wheels or uneven terrain caused a lateral deflection or slippage of the body. At this moment, the steering angle φ of the PDW should been adjusted, in both Task 1 and Task 2, to ensure body balance. As shown in Figs. 8(b) and (f), the angle was adjusted by the VFC without steering commands, which adaptively matches the trajectory of the wheel with the undulations of the terrain. This approach therefore achieves a higher accuracy in linear trajectory tracking than when using IKC, as shown by the auxiliary dashed lines in Figs. 9(a) and (b). More details, the lateral force F_L with VFC, from $F_L = -19.3$ to 27.5 N, is smaller than that with IKC, from $F_L = -4.8$ to 73.4 N, as shown in Figs. 8(d) and (h), especially in Task 2. It is clearly that the application of the PDW in slopes (uneven terrain) is more effective. Note that IKC needs the speed closed-loop control of the front wheels or receiving a steering command to adjust the angle φ.

Remark 3: Between 0 and 13.7 s, the WMR is transitioning

between the flat terrain and slope. After the 13.7-second mark, all the wheels were on the slope, when using VFC. In Task 2, as the slip of the front wheel increased, the angle φ has some wild fluctuations with VFC, indicating that the posture of the body was vibrating when climbing uphill.

In the steering motion case (Task 3), the matching of wheels and terrain is critical, if the PDW is to improve the steering accuracy of the body. As shown in Fig. 8(j), the PDW with the VFC maintains the adjustment of the steering angle φ. Some large adjustments were caused by undulations in the terrain, but the body did not deviate from the track, as shown in Fig. 9(c). The angular velocity ω_b of the WMR can, in practice, be calculated by (20), where $\alpha_1 = 48.3°$, $53.6°$, and $\alpha_2 = 35.3°$, $40°$ are the body initial and final angles, respectively, relative to the defined x-axis in Fig. 9(c).

$$\omega_b = \frac{(360 - \alpha_1 - \alpha_2) \times 2\pi}{360t}. \tag{20}$$

The calculated angular velocities were $\omega_{bVFC} = 0.21$ rad/s, and $\omega_{bIKC} = 0.24$ rad/s. The obtained absolute errors were $e_{\omega IKC} = 0.04$ rad/s, and $e_{\omega VFC} = 0.01$ rad/s, as calculated with the first formula in (21), where i_r is the actual value, and i_d the desired one.

$$\begin{cases} e_{imax} = |i_r - i_d|_{max} \\ \overline{e_i} = \dfrac{1}{n}\sum_{j=0}^{j=n} |i_r - i_d| \end{cases}, \tag{21}$$

where n denotes the number of data and j is the StNum.

The improvement in control accuracy achieved by VFC (relative to IKC) was calculated by (22) as $\delta_\omega = 75\%$, showing the efficacy of VFC in that regard.

$$\delta = \frac{\overline{e}_{IKC} - \overline{e}_{VFC}}{\overline{e}_{IKC}} \times 100\%. \tag{22}$$

To test further performance of the two approaches, five degree downhill was set for the experimental terrain in Task 3, and the triangle in figures points to the beginning. As shown in Figs. 8(i), (j), (k) and (l), the VFC obtains more stable forces by adjusting the velocity and angle than those of IKC.

2) Internal force results: The internal force f_{in} and internal torque T_{in} between the PDW, and body were calculated by (4) and shown in Fig. 10. During linear motions (Task 1 and Task 2), the internal forces between the wheels are considerably reduced, particularly in uneven terrain, which shows the efficacy of the PDW with VFC. As shown in Figs. 10(a), (b), (c) and (d), the force ranges obtained with the two approaches are significantly different: in Task 1, f_{in} ranges from -8.9 to 10.4 N and T_{in} from -3.9 to 4.4 Nm with VFC, while f_{in} ranges from -31.8 to 0.1 N and T_{in} from -0.2 to 8.7 Nm with IKC; in Task 2, f_{in} ranges from -26.0 to 23.5 N and T_{in} from -10.9 to 10.4 Nm with VFC, while f_{in} ranges from -99.0 to -12.8 N and T_{in} from -1.5 to 29.1 Nm with IKC. Considering the force control objective f_{in}= T_{in}= 0, the maximum and average errors are calculated by (21), and shown in Tables I and II.

As summarized in Tables I and II, the increased reductions in internal forces achieved by VFC were $\delta_{f_{in}} = 90.8\%$ and $\delta_{T_{in}} = 84.5\%$ in Task 1, and $\delta_{f_{in}} = 93.3\%$ and $\delta_{T_{in}} = 90.8\%$ in Task 2, when compared with IKC using (22). This shows

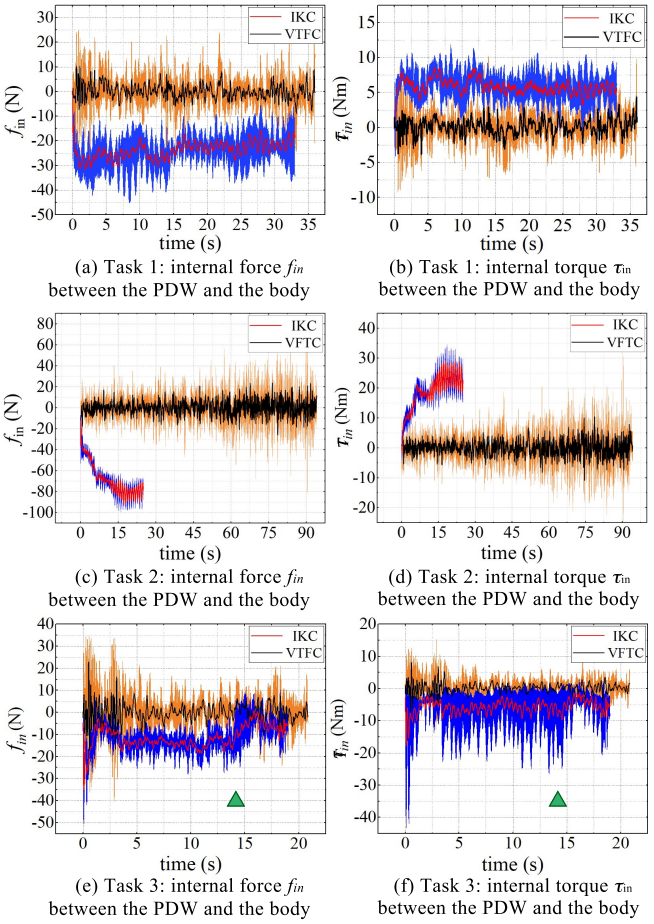

(a) Task 1: internal force f_{in} between the PDW and the body
(b) Task 1: internal torque τ_{in} between the PDW and the body
(c) Task 2: internal force f_{in} between the PDW and the body
(d) Task 2: internal torque τ_{in} between the PDW and the body
(e) Task 3: internal force f_{in} between the PDW and the body
(f) Task 3: internal torque τ_{in} between the PDW and the body

Fig. 10: Internal forces between the PDW and body.

TABLE I: Task 1: Internal Force Errors With IKC and VFC

method	$e_{f_{inmax}}$ (N)	$\overline{e}_{f_{in}}$ (N)	$e_{T_{inmax}}$ (Nm)	$\overline{e}_{T_{in}}$ (Nm)
IKC	31.8	23.8	8.7	5.8
VFC	10.4	2.2	4.4	0.9

TABLE II: Task 2: Internal Force Errors With IKC and VFC

method	$e_{f_{inmax}}$ (N)	$\overline{e}_{f_{in}}$ (N)	$e_{T_{inmax}}$ (Nm)	$\overline{e}_{T_{in}}$ (Nm)
IKC	99.0	72.0	29.1	19.6
VFC	26.0	4.8	10.9	1.8

TABLE III: Task 3: Internal Force Errors With IKC and VFC

method	$e_{f_{inmax}}$ (N)	$\overline{e}_{f_{in}}$ (N)	$e_{T_{inmax}}$ (Nm)	$\overline{e}_{T_{in}}$ (Nm)
IKC	35.0	11.0	17.8	5.7
VFC	22.9	3.0	8.1	1.1

that, using the PDW with VFC is one of the key approaches to eliminate internal forces between wheels.

The obtained results also show that the PDW with IKC provided both a push force f_{in} and a clockwise torque T_{in} to the body. The direction of the torque is mainly caused by the PDW only has a right arm to support additional force. It gave the body extra velocity, which caused a movement offset. On the other hand, as shown in Figs. 9(a) and (b), to travel

the same distance, the WMR with VFC takes 3 s longer than with IKC in Task 1, and 74 s more in Task 2, which results from that the internal forces between the wheels have been reduced. It can be seen that the rover using the PDW with IKC can effectively improve the trajectory tracking speed.

As seen in Figs. 10(e) and (f), during the steering motion (Task 3), the PDW with IKC provided both a push force and a counterclockwise torque to the body. The direction of the torque mainly resulted in a left movement of the body. In the VFC case, the internal forces f_{in} and T_{in} were stable, indicating that the wheel's motion state has effectively matched the terrain undulations, especially in the downhill motion. In Task 3, f_{in} ranges from -19.8 to 22.9 N and T_{in} from -7.4 to 8.1 Nm with VFC, and f_{in} ranges from -35.0 to -1.0 N and T_{in} from -17.8 to -1.1 Nm with IKC. The maximum and average error are calculated with (21), and shown in Table III. As in the previous tasks, a comparison with IKC was performed, which showed that the internal force and internal torque provided by VFC were more reduced by $\delta_{f_{in}} = 72.7\%$ and $\delta_{T_{in}} = 80.7\%$, respectively.

V. Conclusions and Future Work

This paper has presented a pseudo-passive control method that makes one or more wheels driven according to internal forces values between the wheel and the body box to improve coordinated movements of the wheels. The kinematic constraint equations of a PDW were derived. To compensate for force disturbances arising from the deformable soil during wheel–terrain interaction, ADRCs were introduced into the velocity following control (VFC) scheme. The experimental results show that the proposed VFC effectively hold the average internal forces, $\overline{f_{in}}, \overline{T_{in}}$, within small ranges by reducing the forces of the wheel motion plane, the drawbar pull F_{DP} and the lateral force F_L. In the experiments, the PDW with VFC did follow the actual path with improved accuracy compared with that of the inverse kinematics control (IKC), and simultaneously decreasing the internal force f_{in} and internal torque T_{in} by at least 70% and 80% on our trials, respectively. In the slope trials, the climbing speed of the robot using VFC is lower than that of IKC, which shows that internal forces should not always be reduced.

In future work, an intelligent strategy should be studied to control the internal forces more effectively for achieving even better performance.

References

[1] R. Sarkar, K. S. Edgett, D. Ghosh, A. Porwal, and P. Singh, "Tectonic evolution of juventae chasma, mars, and the deformational and depositional structural attributes of the four major light-toned rock exposures therein," *Icarus*, vol. 333, pp. 199–233, 2019.

[2] D. Wheatley, M. Chan, and C. Okubo, "Clastic pipes and mud volcanism across mars: Terrestrial analog evidence of past martian groundwater and subsurface fluid mobilization," *Icarus*, vol. 328, pp. 141–151, 2019.

[3] K. Nagaoka, N. Mizukami, and T. Kubota, "Prediction of tractive limitations of a rigid wheel on loose soil," *Journal of Asian Electric Vehicles*, vol. 10, no. 1, pp. 1583–1590, 2012.

[4] Z. Chen, "A brief talk on implementation of redundant control of control systems [j]," *Process Automation Instrumentation*, vol. 9, 2005.

[5] K. Yoshida and H. Hamano, "Motion dynamics and control of a planetary rover with slip-based traction model," in *Unmanned Ground Vehicle Technology IV*, vol. 4715. International Society for Optics and Photonics, 2002, pp. 275–286.

[6] W. Wang, D. Cheng, and X. Hu, "Dynamic modeling and concerted driving control of liunar rover," in *Proceedings of the 22nd China Control Conference*. Wuhan University of Technology Press, 2003, pp. 152–156.

[7] Z. Wang, H. Wu *et al.*, "Fuzzy variable structure control for concerted driving of lunar rover," in *2003 China Intelligent Automation Conference*. Chinese Association of Automation, 2007, pp. 225–229.

[8] K. Iagnemma and S. Dubowsky, "Traction control of wheeled robotic vehicles in rough terrain with application to planetary rovers," *The international Journal of robotics research*, vol. 23, no. 10-11, pp. 1029–1040, 2004.

[9] P. Lamon and R. Siegwart, "Wheel torque control in rough terrain-modeling and simulation," in *Proceedings of the 2005 IEEE international conference on robotics and automation*. IEEE, 2005, pp. 867–872.

[10] L. Ding, H. Gao, Z. Deng, and Z. Liu, "Slip-ratio-coordinated control of planetary exploration robots traversing over deformable rough terrain," in *2010 IEEE/RSJ International Conference on Intelligent Robots and Systems*. IEEE, 2010, pp. 4958–4963.

[11] H. Gao, K. Xia, L. Ding, Z. Deng, Z. Liu, and G. Liu, "Optimized control for longitudinal slip ratio with reduced energy consumption," *Acta Astronautica*, vol. 115, pp. 1–17, 2015.

[12] B. Guo and Z. Zhao, "On convergence of nonlinear active disturbance rejection for siso systems," in *2012 24th Chinese Control and Decision Conference (CCDC)*. IEEE, 2012, pp. 3507–3512.

[13] Z. Zhao and B. Guo, "On convergence of nonlinear active disturbance rejection control for siso nonlinear systems," *Journal of Dynamical and Control Systems*, vol. 22, no. 2, pp. 385–412, 2016.

[14] Z. Zhao, "Convergence of nonlinear active disturbance rejection control," Ph.D. dissertation, Hefei: University of Science and Technology of China., 2012.

[15] C. Chen, H. Gao, L. Ding, W. Li, H. Yu, and Z. Deng, "Trajectory tracking control of wmrs with lateral and longitudinal slippage based on active disturbance rejection control," *Robotics and Autonomous Systems*, vol. 107, pp. 236–245, 2018.

[16] L. Ding, L. Huang, S. Li, H. B. Gao, H. C. Deng, Y. K. Li, and G. J. Liu, "Definition and application of variable resistance coefficient for wheeled mobile robots on deformable terrain," *IEEE Transactions on Robotics*, vol. 36, no. 3, pp. 894–909, 2020.

[17] H. Qi, B. You, L. Ding, W. Lian, Y. Yuan, J. Li, and H. Gao, "Control strategy for the pseudo-driven wheels of multi-wheeled mobile robots based on dissociation by degrees-of-freedom," *IEEE Access*, vol. 8, pp. 155 477–155 491, 2020.

[18] B. You, H. Qi, L. Ding, S. Li, L. Huang, L. Tian, and H. Gao, "Fast neural network control of a pseudo-driven wheel on deformable terrain," *Mechanical Systems and Signal Processing*, vol. 152, p. 107478, 2021.

[19] Y. Zhao and S. BeMent, "Kinematics, dynamics and control of wheeled mobile robots," in *Proceedings 1992 IEEE International Conference on Robotics and Automation*. IEEE, 1992, pp. 91–96.

[20] L. Ding, "Wheel-soil interaction terramechanics for lunar/planetary exploration rovers: modeling and application," *Harbin Institute of technology*, 2009.

[21] L. Ding, H. Gao, Z. Deng, K. Nagatani, and K. Yoshida, "Experimental study and analysis on driving wheels' performance for planetary exploration rovers moving in deformable soil," *Journal of Terramechanics*, vol. 48, no. 1, pp. 27–45, 2011.

[22] J. Han, "Active disturbance rejection control technique-the technique for estimating and compensating the uncertainties," *National Defense Industry Press, Beijing*, pp. 197–270, 2008.

[23] Z. Gao, "Active disturbance rejection control: a paradigm shift in feedback control system design," in *2006 American control conference*. IEEE, 2006, p. 7.

[24] J. Han, "From pid to active disturbance rejection control," *IEEE transactions on Industrial Electronics*, vol. 56, no. 3, pp. 900–906, 2009.

[25] Z. Sun, T. Zhang, H. Zhang, Y. Jia, H. Zhang, J. Chen, X. Wu, and Z. Shen, "The technical design and achievements of chang'e-3 probe," *Scientia Sinica Technologica*, vol. 44, no. 4, pp. 331–343, 2014.